All-optical hyperpolarization of electron and nuclear spins in diamond

B. L. Green,[1,*] B. G. Breeze,[1] G. J. Rees,[1] J. V. Hanna,[1] J.-P. Chou,[2] V. Ivády,[2,3] A. Gali,[2,4,†] and M. E. Newton[1,‡]

[1]*Department of Physics, University of Warwick, Coventry CV4 7AL, United Kingdom*

[2]*Wigner Research Centre for Physics, Hungarian Academy of Sciences, P.O. Box 49, 1525 Budapest, Hungary*

[3]*Department of Physics, Chemistry and Biology, Linköping University, SE-581 83 Linköping, Sweden*

[4]*Department of Atomic Physics, Budapest University of Technology and Economics, Budafoki út 8., 1111 Budapest, Hungary*

(Received 14 February 2017; revised manuscript received 28 June 2017; published 1 August 2017)

Low thermal polarization of nuclear spins is a primary sensitivity limitation for nuclear magnetic resonance. Here we demonstrate optically pumped (microwave-free) nuclear spin polarization of ^{13}C and ^{15}N in ^{15}N-doped diamond. ^{15}N polarization enhancements up to −2000 above thermal equilibrium are observed in the paramagnetic system N_s^0. Nuclear spin polarization is shown to diffuse to bulk ^{13}C with NMR enhancements of −200 at room temperature and −500 at 240 K, enabling a route to microwave-free high-sensitivity NMR study of biological samples in ambient conditions.

DOI: 10.1103/PhysRevB.96.054101

I. INTRODUCTION

The enhancement of nuclear polarization is of great importance to nuclear magnetic resonance (NMR) experiments, where the primary sensitivity limit is caused by the small thermal population differences of nuclear spin levels. The development of a general nuclear hyperpolarization technique at arbitrary fields would enable measurements of biomolecules and reaction dynamics that were not accessible by the present techniques while decreasing routine NMR measurement times by orders of magnitude [1]. Several approaches to dynamic nuclear polarization (DNP) processes have been demonstrated that enhance nuclear spin polarization; however, the majority are limited to specific fields [2–5], low temperatures [6,7], specific molecules [8], or require microwave irradiation of the sample [8,9]. Low temperature is particularly problematic for liquid-state biological samples, where freezing leads to a loss of spectral resolution [10]. Recently, microwave-free optically pumped DNP (OPDNP) of a diamond containing a high concentration of the negatively charged nitrogen vacancy center (NV^-) was demonstrated [11]; however, the electron-nuclear transfer mechanism is not well-understood.

In this article, we demonstrate the electronic spin polarization of two $S = 1/2$ paramagnetic nitrogen centers, N_s^0 (substitutional nitrogen [Fig. 1(a)]) and N_3V^0 (vacancy with three nearest-neighbor nitrogen), in a ^{15}N-doped synthetic diamond with an NV^- concentration $<10^{-3}$ of N_s^0. Upon illumination, neighboring ^{13}C and ^{15}N nuclei incorporated in these defect centers are spin-polarized, with ^{15}N polarization enhancement of >2000 over thermal equilibrium observed. Nuclear spin polarization is shown to diffuse to the bulk ^{13}C, leading to microwave-free OPDNP enhancements of −200 at room temperature and −500 at 240 K. We propose a possible spin polarization mechanism supported by *ab initio* calculations.

N_s^0 and N_3V^0 point defects in diamond

The N_s^0 and N_3V^0 point defect centers in diamond each possess a $\langle 111 \rangle$ C_{3v} symmetry axis [Fig. 1(a)], and thus they possess four symmetry-related orientations within the T_d diamond lattice. Both centers are $S = 1/2$ in the ground state (GS): unpaired electron probability density is primarily localized on the carbon atom(s) nearest neighbor to the vacancy [12], yielding small nitrogen hyperfine interactions [12,13]. The primary sample investigated was doped with ^{15}N ($I = 1/2$), and therefore each orientation of N_s^0 (N_3V^0) contributes a maximum of two (eight) resonance lines to an electron paramagnetic resonance (EPR) spectrum.

Due to its role both as one of the most abundant impurities in diamond and its potential as a donor, the electronic structure of N_s^0 has been studied extensively. It is well established from thermoconductivity measurements that the ground state lies approximately 1.7 eV below the band gap [14]. Photoconductivity measurements report cut-on thresholds at approximately 1.9–2.2 eV [15,16] [see the underlying ramp of Fig. 1(b)]. There is some suggestion that N_s may also possess an acceptor level with a transition energy of approximately 4.6 eV [17,18].

The electronic structure of N_3V is not definitively known. In the neutral charge state, the ground-state and excited-state characters ($^2A_1$ and ^2E, respectively) have been experimentally verified via optical characterization of the N3 zero-phonon line (ZPL) transition at 3.0 eV [19,20] [ZPL visible in Fig. 1(b)] and EPR of the ground state [21–23]. Some confusion has arisen due to the presence of additional optical transitions (N2,N4), which may arise at the same center [21]. The N2 and N3 transitions have been correlated by over an order of magnitude in intensity, and hence N2 appears to be associated with N_3V^0 [21]. The weak N2 absorption has led to a suggestion that it arises from a symmetry-forbidden dipole transition ($A_1 \leftrightarrow A_2$ in C_{3v} symmetry) [21]; however, it is not possible to generate the $^2A_2$ state in the "vacancy-cage" electronic model (explicitly treating only those orbitals directly pointing into the vacancy) typically used to treat vacancy-type defects in diamond [24,25]. Theoretical analysis has suggested the presence of an additional one-electron level outside the vacancy, weakly bound to the defect center [26]: the weak N2 transition is then explained by the difference in wave-function localization between the ground and excited

*b.green@warwick.ac.uk

†gali.adam@wigner.mta.hu

‡Corresponding author: m.e.newton@warwick.ac.uk

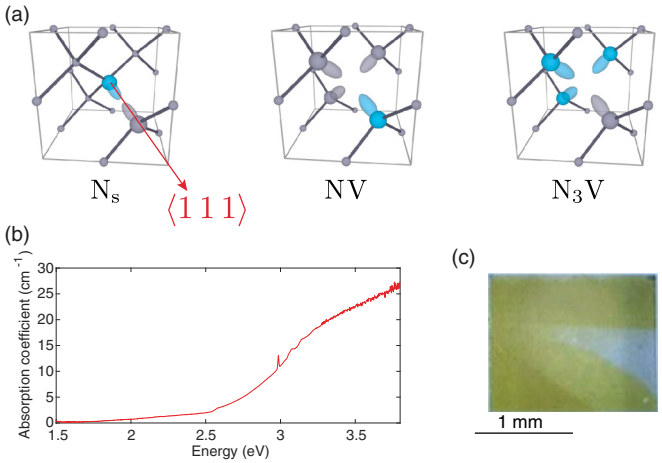

FIG. 1. (a) Atomic structures of N_s (left), NV, and N_3V . In all cases, the unpaired electron probability density is localized primarily in the carbon orbitals (gray). (b) The uv-vis absorption spectrum of the sample at 80 K. (c) Photograph of the sample used for this study. Nitrogen inhomogeneity is evident by the variation in yellow color saturation in the different growth sectors. Counterintuitively, the highest concentration of N_3V is found in the clear sector: this is because the level of nitrogen aggregation is highest in the high-nitrogen sector, leading directly to a reduction of the yellow color.

states. Recent experimental results suggest that the N2 and N3 transitions may not correlate in all circumstances [27]. Photochromism measurements indicate that N_3V may also be stable in the negative charge state [12,28], though no spectroscopic signatures have been identified with N_3V^- .

II. METHODS

A. Sample

The ^{15}N-enriched sample [Fig. 1(c)] used for EPR, NMR, and optical studies was grown using the isotopically enriched high-pressure–high-temperature (HPHT) technique described in [29]. Postsynthesis, the sample contained average substitutional nitrogen concentrations of $[^{15}N_s^0] = 80(2)$ ppm and $[^{14}N_s{}^0] = 4(3)$ ppm, respectively: the doping varied by over an order of magnitude in different sectors [Fig. 1(b)]. The sample was neutron-irradiated to a dose of 5×10^{17} neutrons cm^{-2} and subsequently annealed under a nonoxidizing atmosphere for 15 h at 1500 °C, before finally being annealed under high pressure at a nominal temperature of 1900 °C for 1 h. This processing regime generated a total concentration of $[^{15}N_3V^0] = 1.6(2)$ ppm and residual substitutional nitrogen concentrations of 20 ppm $[^{15}N_s^0]$ and 5 ppm $[^{15}N_s^+]$, respectively. Additionally, 40 ppm of nitrogen was measured in nearest-neighbor pairs $((N_s - Ns)^0$, called *A* centers) and approximately 15 ppm was estimated in $^{15}N_4V^0$ form by infrared absorption measurements. The sample was polished in order to remove the seed crystal and to provide a flat reference face (within 1° of ⟨110⟩). Inhomogeneities in the uptake of nitrogen during growth are visible in the sample when viewed under a microscope [Fig. 1(b)]. The use of ^{15}N ($I = 1/2$) during synthesis greatly simplifies the electron paramagnetic resonance (EPR) spectra compared to ^{14}N ($I = 1$) due to the absence of nuclear quadrupole interactions [12] and reduction of hyperfine multiplicity.

B. EPR measurements

EPR measurements were performed on a Bruker EMX X-band spectrometer equipped with an ER4109HS cylindrical resonator and an ER041XG microwave bridge: measurements were collected at nonsaturating microwave power. The sample was mounted onto the end of a Rexolite tube, and laser light was delivered via a ø1 mm optical fiber fed through the bore of the Rexolite tube.

C. NMR measurements

The static ^{13}C solid-state NMR measurements were completed at 7.04 T using a Bruker Avance III HD spectrometer. A 5 mm low-temperature static probe was used to produce an 80 kHz $\pi/2$ pulse, which was calibrated on CH_3OH(l). The diamond was mounted into a 3.2 mm ZrO_2 rotor with the ⟨111⟩ axis parallel to B_0. The sample was held in place using a ø0.2 mm optical fiber fixed into the cap position.

D. *Ab initio* calculations

Theoretical calculations were performed by using density functional theory (DFT). A 512-atom supercell diamond with 370 eV of plane-wave cutoff energy and Γ-point sampling of the Brillouin zone was used in the calculations. We applied an HSE06 [30] hybrid density functional, which is capable of providing accurate band gap and defect levels in diamond within 0.1 eV to experiment [31]. The electronic transition (zero-phonon-line energy) was calculated by the constrained DFT approach [32]. The imaginary part of the frequency-dependent dielectric matrix, which represents the absorption spectrum without excitonic effects, was calculated without including local field effect [33]. The defect's charge transition level, i.e., $(-|0)$, can be determined by the defect formation energies of the neutral and negatively charged states [34]. The finite-size effects of supercells associated with electrostatic interactions were corrected using the scheme developed by Freysoldt *et al.* [35,36]. We calculated the zero-field splitting parameters associated with the electron spin dipole-dipole interaction using our in-house-built code [37,38]. In the calculation of the hyperfine coupling constants, the core spin polarization within the frozen valence approximation is taken into account [39,40].

III. RESULTS

A. EPR

1. *Optically pumped spin polarization*

A typical low-temperature EPR spectrum of the sample with applied magnetic field $B_0 \| \langle 111 \rangle$ is given in the upper half of Fig. 2(a). The nitrogen hyperfines of $^{15}N_s^0$ are labeled as follows: 1 and 4 arise from transitions at the field-parallel orientation (with the ⟨111⟩ symmetry axis of the defect parallel to the applied magnetic field); 2 and 3 arise from the three orientations whose symmetry axes are at 109° to the applied magnetic field. For each orientation, the low- and high-field resonances correspond to the transitions $|-,-\rangle \leftrightarrow |+,-\rangle$ and

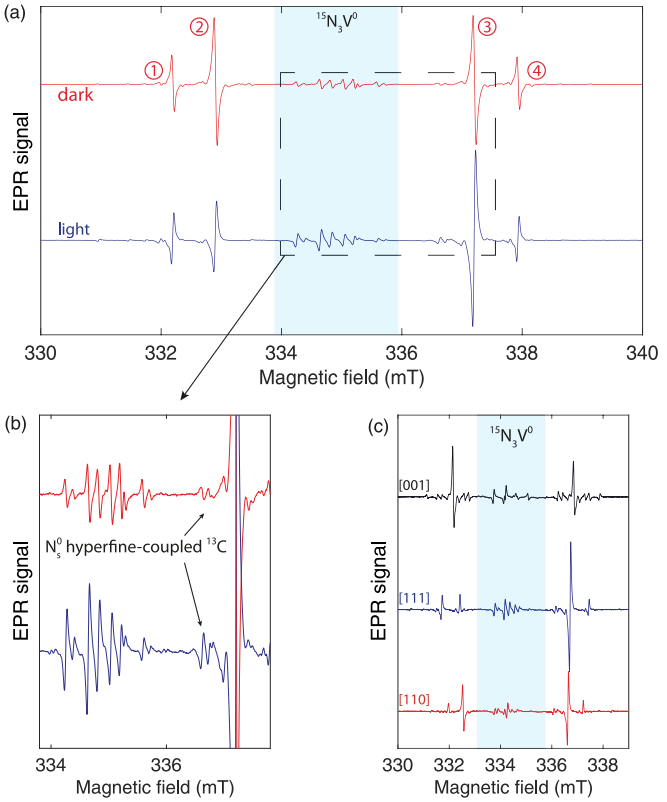

FIG. 2. (a) EPR spectra collected without (top) and with illumination by 80 mW of light at 532 nm (2.33 eV) with the sample at 85 K and the external magnetic field $B_0 \| \langle 111 \rangle$. The two visible systems are $^{15}N_3V^0$ (shaded) and $^{15}N_s^0$ (all other lines, nitrogen hyperfine transitions numbered): inversion of the lines under illumination indicates electron spin polarization, and the change in relative intensity of different lines is due to nuclear spin polarization. The panel highlights nuclear polarization of $^{15}N_3V^0$ and ^{13}C coupled to $^{15}N_s^0$. (b) EPR spectra along three high-symmetry directions under illumination from 70 mW of 532 nm light at a sample temperature of 85 K.

$|-,+\rangle \leftrightarrow |+,+\rangle$, respectively, in the basis $|m_S, m_I\rangle$. (m_S, m_I are eigenstates of the spin Hamiltonian only for the field-parallel orientation; the label is employed for convenience.)

The more complex spectrum originating at $^{15}N_3V^0$ is highlighted in [Fig. 2(a)]. The straightforward assignment of spectral lines to orientations and transitions is not possible in this case due to overlapping spectra from different orientations [12].

At temperatures below approximately 120 K, *in situ* optical illumination results in electron spin polarization of both N_s^0 and N_3V^0 in field-parallel and non-field-parallel orientations [Fig. 2(a) lower spectra, electronic polarization identified by spectral inversion]. The constituent ^{15}N nuclei are spin-polarized in both centers (identified by changes in relative intensity of different transitions within a single orientation of a center, e.g., transitions 2 and 3), as are proximal ^{13}C (1.1 % abundance). The observed spin polarization depends strongly on the orientation of the external magnetic field B_0 [Fig. 2(c)]. The effect is strongest with $B_0 \| \langle 111 \rangle$, where all detectable paramagnetic species exhibit both electronic and nuclear spin polarization, and it is weakest for $B_0 \| | \langle 001 \rangle$, where nuclear

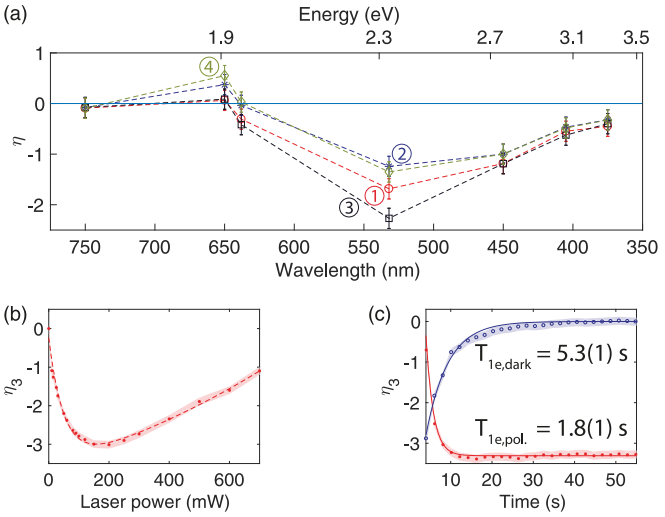

FIG. 3. (a) Dependence of EPR enhancement η on laser wavelength for each of the $^{15}N_s^0$ hyperfines at 85 K [labeled as in Fig. 2(a)]. Measurements taken at 80 mW optical power at the sample (10.2 W cm^{-2}). (b) EPR enhancement as a function of power at 520 nm and 50 K. (c) Buildup and decay of electron polarization at 50 K when illumination is switched on and off, respectively.

polarization is detectable on the ^{15}N and ^{13}C hyperfines of $^{15}N_s^0$ and the primary hyperfines of $^{15}N_3V^0$.

The polarization excitation mechanism is highly broadband, with electron and nuclear enhancements measured for 750–375 nm (1.65–3.31 eV) [Fig. 3(a)]. EPR enhancements $\eta = (I_{\text{light}} - I_{\text{dark}})/I_{\text{dark}}$ up to a factor of $\eta = -3$ were measured using 150 mW (19 W cm^{-2}) at 532 nm (2.33 eV) and a sample temperature of 50 K. As the optical power is increased, the polarization saturates before decreasing [Fig. 3(b)]: it is postulated that this decrease can be accounted for primarily by a mixture of sample heating and photoionization of N_s^0 [12].

2. *Polarization lifetime*

The characteristic lifetimes of the electronic polarization buildup and decay ($T_{1e,\text{pol}}$ and $T_{1e,\text{dark}}$, respectively) were measured by monitoring transition 3 [see Fig. 2(a)] as the illumination was applied and removed. At a sample temperature of 50 K, values of $T_{1e,\text{pol}} = 1.8(1)$ s and $T_{1e,\text{dark}} = 5.3(1)$ s were determined [Fig. 3(c)]. Temperature-dependent spin-lattice lifetime measurements without illumination yielded $T_{1e} = 0.4(6)$ s at 100 K and an extrapolated lifetime of 2 s at 50 K. We observe electronic polarization at approximately 120 K [$T_{1e} = 0.35(5)$ s] and below, suggesting that the observation of electron polarization is contingent on $T_{1e,\text{pol}} \lessapprox T_{1e}$.

In addition to the fast buildup and decay of electronic polarization, a second decay is observed over time scales of minutes after optical excitation is removed: this indicates that ^{15}N nuclear polarization persists beyond the electronic polarization. Immediately following the removal of illumination, the ratio of observed nuclear polarization to thermal equilibrium, $\epsilon_{^{15}N}$, was measured as -2000, corresponding to $\approx 1/3$ of electron thermal polarization. The nuclear polarization is strongest in the field-parallel orientation of N_s^0, where m_S and m_I are eigenstates of the N_s^0 spin system (Fig. 4).

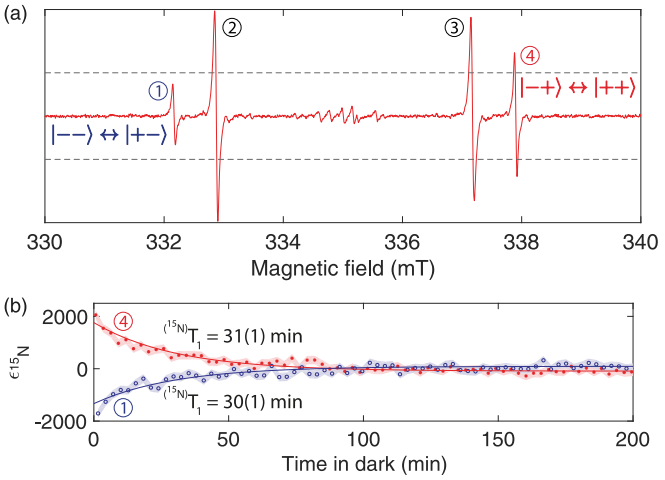

FIG. 4. (a) EPR spectrum taken approximately 30 s after illumination is switched off. Field-parallel hyperfine $^{15}N_s^0$ transitions 1 and 4 correspond to $|m_I\rangle = -1/2$ and $+1/2$, respectively (transitions given in the figure in the basis $|m_S m_I\rangle$): intensity difference is due to ^{15}N nuclear polarization. Dotted line indicates equilibrium intensity of transitions 1 and 4. (b) Nuclear polarization of field-parallel $^{15}N_s^0$ hyperfines 1 and 4 as a function of time after optical excitation removed: equilibrium is reached with a characteristic lifetime of 31(1) min at 50 K. A nuclear polarization of $\epsilon_{^{15}N} \approx -2000$ over thermal equilibrium is observed. Hyperfines 2 and 3 equilibrate with a lifetime of 42(3) min. The data have been corrected for a slow charge-transfer process (see [43]), and they are interpreted in terms of electron migration to a population of nuclear-polarized N_s^+ (see the main text).

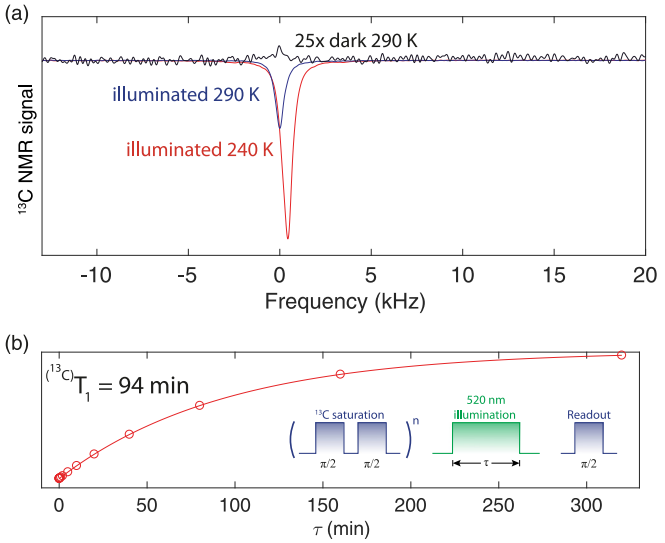

FIG. 5. (a) Single shot ^{13}C NMR spectra at 7.04 T (400 MHz proton frequency). Illuminated spectra were collected following illumination at 520 nm (2.38 eV); the dark spectrum was collected after 86 h at field. (b) Room-temperature bulk ^{13}C polarization buildup, collected via saturation recovery using a train of saturating $\pi/2$ pulses (to destroy any polarization between each experimental shot) and illuminating for a time τ (see the inset).

The spin lifetimes of nuclei in strongly-hyperfine-coupled paramagnetic systems are typically limited by the lifetime of the associated electron: nuclear-spin lifetimes have been extended in silicon and diamond by actively "removing" the unpaired electron from such a system for a given duration, then returning it for readout via the electron [41,42]. We therefore interpret our effective nuclear T_1 in terms of a highly polarized population of N_s^+, which is nonparamagnetic and therefore can sustain long nuclear-spin lifetimes. Charge transfer between defect centers in the sample yields $^{\uparrow}N_s^+ + X^- \rightarrow {}^{\uparrow}N_s^0 + X^0$, with $\uparrow$ indicating nuclear polarization: the N_s^0 defects are thus formed by migration of an electron to a prepolarized N_s^+ center, and they are subsequently read out via EPR of the electron. The observed effective lifetime $^{15}N T_1 = 30(1)$ min is a lower limit for the "protected" (nonparamagnetic) ^{15}N nuclei, as it must include contributions both from the nuclear lifetime and the characteristic charge-transfer time of the population. During the time-series measurement [Fig. 4(a)], we observe an exponential drop in the total N_s^0 concentration [43], indicating that at least two distinct populations exist within the sample: those centers that provide a source of $^{\uparrow}N_s^+$ and equilibrate to N_s^0 over time, and those that are initially in the N_s^0 state and equilibrate to N_s^+.

B. NMR

EPR measurements are restricted to readout of ^{13}C nuclei within several lattice spacings only—at distances beyond approximately 6 Å, the electron-nuclear dipolar coupling becomes unresolved inside the envelope of the EPR linewidth. NMR measurements are therefore required to determine if the polarization local to the defect centers is transferred to the bulk 1.1% ^{13}C nuclei.

Single-shot ^{13}C NMR measurements collected with the sample under *in situ* optical illumination at 520 nm (2.38 eV) indicate that the nuclear-spin polarization extends beyond the local nuclei and into the bulk [Fig. 5(a)]. The characteristic time for this process is 94 min: this is too slow for an electronic process, and hence it is proposed to be mediated by nuclear-spin diffusion from the polarized shell around the paramagnetic centers. Bulk OPDNP enhancements of $\epsilon_{^{13}C} = -200$ were measured at room temperature, and $\epsilon_{^{13}C} > -500$ at 240 K, leading to experimental speedup factors of 40 000 and 250 000, respectively. An additional factor of 4 is gained by the reduction in longitudinal spin lifetime under optical illumination (from $(^{13C})T_{1,\mathrm{dark}} > 8$ h to $(^{13C})T_{1,\mathrm{light}} \approx 1.5$ h).

C. Samples with different defect concentrations

To verify whether or not the presence of N_3V^0 was required in order to observe the present polarization effects, and also to rule out NV-related effects, a further four samples were measured under the same EPR conditions as the primary sample. A total of three samples (samples 1–3, including the primary sample—see Table I) were grown simultaneously in the same reaction volume, and hence they have the same nitrogen isotopic enrichment: of these, one was measured as-grown, one was electron-irradiated and annealed to produce NV^- before measurements; the primary sample is described in Sec. II A. Samples 4 and 5 were HPHT-grown and natural, respectively. Optically pumped EPR measurements of the four alternative samples failed to exhibit any detectable electron

TABLE I. Summary of the samples tested for the presence of electron or nuclear polarization under the same experimental conditions as the primary sample (sample 1). Samples 1–3 were grown simultaneously; sample 5 is a natural sample.

Sample	Enrichment	Defect concentration (ppm)					
	^{14}N: ^{15}N	$N_s^{0/+}$	NV^-	N_3V^0	N_2^0	N_4V^0	NMR measured?
1	5: 95	25	<0.01	1.6	40	15	Y
2	5: 95	125					N
3	5: 95	120	10				Y
4	15: 85	38					N
5	99.6: 0.4	2	0	30			Y

spin polarization of N_s^0 or N_3V^0 . Optically pumped NMR measurements of samples 3 and 5 also failed to detect any nonthermal-equilibrium ^{13}C nuclear polarization.

IV. DISCUSSION

A. Polarization transfer

Two distinct processes can be identified in this sample under illumination: the generation of electron and nuclear spin polarization, and the transfer of that polarization out to bulk nuclei. Our EPR measurements demonstrate electronic polarization occurring at N_3V^0 and N_s^0 on time scales orders of magnitude faster than the bulk nuclear polarization: we therefore presume that these centers are the source of the polarization. However, we will not initially consider the detail of how the spin polarization is generated, but simply deal with its transfer to bulk nuclei.

Several mechanisms exist to transfer polarization from electrons to nuclei, though the typical mechanisms encountered in solids (the solid, cross, and thermal effects [44,45], and Hartmann-Hahn resonance [46]) require microwave driving of the electron spin(s)—absent in our NMR experiments. We observe nuclear spin polarization at both 0.34 and 7.04 T, and therefore we assume that no resonance coupling of the nuclear and electron spins is required for polarization transfer from electron to nuclei. EPR measurements indicate high levels of nuclear polarization local to the paramagnetic center (within three lattice spacings); however, these nuclei cannot efficiently couple to bulk nuclei due to the local field induced by the electron.

Electron-spin polarization may be transferred to bulk nuclei via a three-spin electron-electron-nucleus exchange process (i.e., $|+,-,+\rangle \rightarrow |-,+,-\rangle$ in the basis $|m_{S_1},m_{S_2},m_I\rangle$), with the condition that the difference of the dipolar-coupled electron resonance frequencies must equal the nuclear Larmor frequency $|\Delta\omega_S| = |\omega_1 - \omega_2| = |\omega_I|$. At 0.34 and 7.04 T, the ^{13}C Larmor frequency $\omega_{^{13}C} = 3.64$ and 75.3 MHz, respectively. The spin Hamiltonian values for $^{15}N_3V^0$ and $^{15}N_s^0$ [12,13] are such that a large number of frequencies between 0 and 100 MHz are generated at both field strengths (Fig. 6) (see the Supplemental Material for further details [43]), facilitating polarization transfer to weakly coupled, distant nuclei: net bulk polarization will proceed by resonant spin diffusion.

The above model is sensitive to both the spatial proximity of paramagnetic centers and also to the spin Hamiltonian parameters of the centers (i.e., the "type" of center, and its interaction with the applied magnetic field). Statistical modeling of relative positions at the present concentrations indicates that between 5% and 20% of defect center pairs have a separation of 1.7–4.7 nm (see [43] for an exploration of model sensitivity to defect center orientation and separation, and magnetic-field strength), corresponding to dipolar coupling frequencies of 0.5–10 MHz. This distribution of dipolar couplings will yield a population of centers that are difficult to observe in EPR but will generate additional resonance frequencies (and hence $\Delta\omega_S$), increasing the probability of meeting the polarization transfer matching condition $\Delta\omega_S = |\omega_I|$. Additionally, the small difference in g-values between the two defects means these conditions will be met for a large range (approximately 0.3 to >14 T) of magnetic-field strengths.

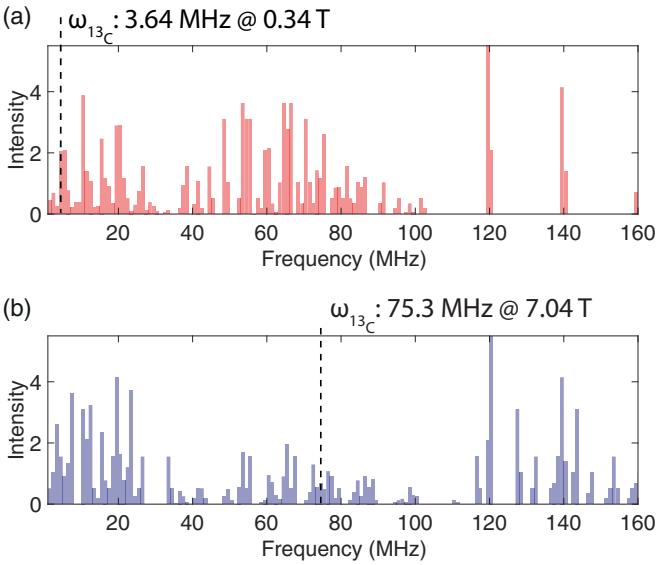

FIG. 6. Difference frequencies generated by the "allowed" ($\Delta m_S = \pm 1$; $\Delta m_I = 0$) electron transitions of a $^{15}N_s^0 - {}^{15}N_3V^0$ pair for $B\|\langle 111\rangle$ at (a) 0.34 ($\omega_{^{13}C} = 3.64$ MHz) and (b) 7.04 T ($\omega_{^{13}C} = 75.3$ MHz) with an isotropic dipolar coupling of 0.5 MHz: stronger couplings will increase the number of frequencies generated and enhance polarization transfer. ^{13}C hyperfine couplings have been ignored in the model.

B. Polarization generation

1. *Electronic structure of N_s^0 and N_3V^0*

We turn our attention now to the initial generation of the polarization itself. There have been several reports of OPDNP in diamond, however we are aware of only two reports (from the same group) that study all-optical diamond DNP [11,47]: in both cases, the effect is attributed to polarization transfer from NV^- . The NV^- concentration in the present sample is below EPR detection limits (≈10 ppb), even when measured under illuminated (spin-polarized) conditions. Optically pumped measurements of four other samples, both ^{14}N- and ^{15}N -doped with a range of NV^- concentrations (Table I), failed to exhibit any detectable electron spin polarization: thus we do not attribute the present mechanism to NV^- and must instead consider the other defects and processes present.

The accepted electronic structure of N_s^0 [43] places only one level (of a_1 symmetry) in the band gap: thermoconductivity measurements give the ionization threshold at 1.7 eV, whereas photoionization is subject to a substantial Stokes shift and starts at approximately 1.9–2.2 eV [15,16]. Similarly, the ground state of N_3V^0 has only one hole (also a_1 symmetry), with the excited-state transition at 3.0 eV [48]. Additional transitions at 2.6 and 3.6 eV are associated with N_3V^0 : DFT studies of N_3V^0 suggest that they may arise from an additional hydrogenic-type state ($N_3V^+ + e^-$), yielding another a_1 state and potentially enabling high-spin ($S > 1/2$) states [26]. Nevertheless, we expect the optical threshold for N_3V to be greater than 2.6 eV, contrary to the ≈1.9 eV observed here [Fig. 3(a)]: these limitations preclude the typical internal singlet-triplet intersystem crossing and level anticrossing polarization mechanisms observed in diamond and SiC [5,49,50]. Both N_s^0 (including $^{15}N_s^0$ [51]) and N_3V^0 have been studied independently and extensively under optical excitation [21,52], and no spin polarization of either system has been reported. The other high-abundance defects in this sample (N_2, N_4V) have no reported optical transitions below 4 eV, and the optical absorption spectrum of this sample contains only N_s^0 and N_3V^0 [43].

Based on the above argument, we conclude that the observed spin polarization is not due to an intrinsic property of either N_s^0 or N_3V^0 . The simultaneous observation of spin polarization in two well-characterized, optically non-spin-polarizable defects suggests a common mechanism. The data allow us to place constraints on such a mechanism: we suppose the same mechanism is responsible for polarization at both 0.34 and 7.04 T, and therefore it is relatively insensitive to magnetic-field strength. Additionally, the mechanism must be capable of spin-polarizing electrons and nuclei in multiple systems simultaneously.

2. *Electronic structure of N_3V^-*

Experimentally, optical illumination at >1.9 eV is sufficient to ionize N_s^0, whereby we hypothesize that N_3V^0 centers can capture the carriers and become negatively charged, N_3V^- [12,28]. We would therefore expect N_s^0 and N_3V^0 concentrations to decrease on optical illumination ($N_s^0 + N_3V^0 \rightarrow N_s^+ + N_3V^-$). However, we find that N_s^0 and N_3V^0 concentrations both increase under illumination at 2.33 eV [12], suggesting that the reverse charge-transfer process is occurring ($N_s^+ + N_3V^- \rightarrow N_s^0 + N_3V^0$). This is supported by our DFT calculations (see [43] for further details), which predict the adiabatic acceptor level of N_3V^0 at 1.85 eV below the conduction-band minimum (CBM), such that proximal defect pairs of N_s and N_3V will equilibrate into positive and negative charge states, respectively. We therefore conclude that when exposed to optical illumination of $\hbar\omega > 1.9$ eV, both the forward and reverse processes are occurring and the sample is therefore in a metastable equilibrium ($N_s^+ + N_3V^-$) ↔ ($N_s^0 + N_3V^0$).

Further *ab initio* calculations indicate that the CBM states split near the N_3V^- defect due to the perturbation potential of the defect. Our calculations indicate that the excited state of N_3V^- is a bound exciton and includes resonant conduction-band states [Fig. 7(a)]. The calculated radiative lifetime of the singlet ^1E is about three times longer than that of $^1A_1$, thus these states provide a route for differential decay processes. The $^3E^*$ ($^3A_1^*$) can couple to the $^1A_1$ ($^1E^*$) excited state by transverse spin-orbit coupling [Fig. 7(b)]. The corresponding spin substates of $^3E^*$ and $^3A_1^*$ are also coupled by transverse spin-orbit coupling.

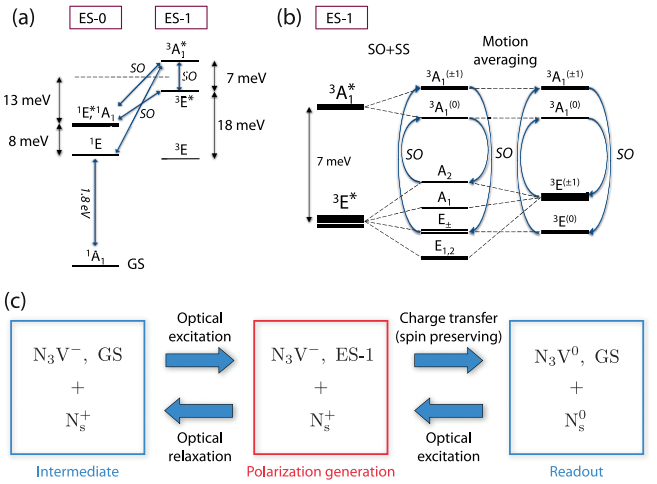

FIG. 7. (a) Fine structure of N_3V^- excited states, including the three lowest-energy triplets (ES-1) and singlets (ES-0). The higher-energy A_1 and E states are marked by $*$. Excited states are resonant with the local conduction-band minimum. (b) Spin-orbit (SO) coupling effects in the closest pair of $^3A_1^*$ and $^3E^*$ states. Blue arrows indicate transverse spin-orbit coupling. At room temperature, phonon-induced spin-conserving transitions may average out the spin-orbit splitting of the states driven by axial spin-orbit coupling and electron spin-spin (SS) couplings. (c) Possible model for spin-polarization generation. Continuous optical excitation and relaxation causes defect pairs to oscillate between different charge and excitation states. Spin-orbit interactions generate spin polarization in the excited state of N_3V^-; thermal excitation out of this state produces a spin-polarized current that is captured by N_s^+, leading to spin-polarized N_s^0 and N_3V^0.

Upon applying an on-axis (positive) external magnetic field, the $^3A_1^*$ and $^3E^*$ states will be slightly $m_S = +1$ and -1 polarized, respectively, due to the asymmetry of the spin-orbit coupling between the different spin states. The asymmetry, and thus the spin polarization, increases with the magnetic-field strength (see [43] for the parameters used in the calculation). Due to the transverse spin-orbit coupling and the differential decay from the singlet states, the $^3A_1^*$ state has a longer lifetime than the $^3E^*$ state. As a consequence of a possible thermal ionization of the N_3V^- excited state, the electron spin is left spin-up polarized on N_3V^0 and a spin-polarized carrier is ejected into the conduction band that can be captured by a proximate N_s^+ defect, thus spin-polarized N_s^0 will form [Fig. 7(c)].

C. Complete mechanism

The proposed polarization generation mechanism, based on the continuous ionization and electron recapture at N_3V, can account for the electronic spin polarization of both N_s^0 and N_3V^0 under optical illumination (and without microwave driving). Similarly to the polarization transfer mechanism

discussed in Sec. IV A, the generation mechanism also requires the N_s^0 and N_3V^0 centers to be in close proximity to prevent spin-lattice interactions causing depolarization of the spin-polarized current [53,54]. Under the proposed model, each defect pair in close proximity (of the order of <3 nm) is therefore capable of both generating electronic polarization by ionization and transferring it to the bulk nuclei via three-spin interactions.

D. Polarization efficiency

The efficiency of the polarization mechanism is difficult to estimate: in our measurements, 40% polarization of 5% population is indistinguishable from 10% polarization of 20% population. The sample under study is highly inhomogeneous, with at least three optically distinguishable nitrogen concentrations and two distinct concentrations visible in EPR spectra (determined by line-shape analysis). If the polarization mechanism is dependent on interaction between N_s^0 and N_3V, then we expect it to occur in only the higher nitrogen sectors (upper limit 40% of the sample). At room temperature ($T_{1e} \approx 1$ ms), no electron polarization is visible in the EPR spectra, and the upper limit on ^{13}C polarization is therefore given by the ratio of the Boltzmann polarizations $\propto \mu_e/\mu_{^{13}C} \approx$ 2600: enhancements of -200 correspond to an effective homogeneous efficiency of approximately 8%. Enhancements of |200| match those achieved in OPDNR measurements of diamonds containing high concentrations of NV under similar optical power densities [11].

Our measurements yield similar enhancements to conventional microwave-driven DNP measurements on N_s^0 in diamond ($\epsilon_{^{13}C} = 140$) [55] and microwave-free OPDNP measurements exploiting NV^- centers ($\epsilon_{^{13}C} = 200$) [11]. Enhancements of $\approx 2 \times 10^5$ have been observed for optically pumped microwave-driven DNP using NV^- at low fields [9], and approximately 45 at high field via sample shuttling [56]: the primary advantage of the present work is projected field-insensitivity without the requirement for expensive high-frequency microwave components (>200 GHz), cryogenics, or sample shuttling at typical NMR fields.

V. CONCLUSION

Our results show that optical pumping can induce electron and nuclear polarization in two paramagnetic systems in diamond with negligible NV^- concentration. NMR measurements with *in situ* illumination show that the nuclear polarization diffuses out to the bulk ^{13}C, leading to OPDNP enhancements of up to -500 at 240 K. The two systems involved, $^{15}N_s^0$ and $^{15}N_3V^0$, have only $S = 1/2$ states accessible, and hence the standard internal triplet intersystem crossing or level anticrossing mechanisms for solid-state polarization [5,50] cannot be responsible here. Our DFT calculations have indicated the presence of a previously unidentified high-spin state in the excited state of N_3V^-. Furthermore, it may be possible for this state to emit a spin-polarized current, spin-polarizing proximal defects. Electron spin polarization is transferred to bulk nuclei by anisotropic three-spin exchange, with a large set of frequencies generated by the interaction between $^{15}N_s^0$ and $^{15}N_3V^0$. Our study implies that engineered synthetic nanodiamonds with concentrations designed to maximize the bulk nuclear polarization would provide a general platform for optical hyperpolarization of a target sample via existing transfer mechanisms such as cross-polarization [57] and Hartmann-Hahn resonance [58], enabling the study of new biological and dynamical systems without the requirement for sample shuttling, low temperature, or microwave irradiation.

ACKNOWLEDGMENTS

The authors thank H. Fedder, M. W. Doherty, M. W. Dale, and C. J. Wedge for helpful discussions. We acknowledge funding from the Engineering and Physical Sciences Research Council (Grants No. EP/M013243/1 and No. EP/J500045/1), the Gemological Institute of America, and the EU Commission (FP7 DIADEMS Project No. 611143). We thank De Beers Technologies for provision of samples.

[1] R. G. Griffin and T. F. Prisner, Phys. Chem. Chem. Phys. **12**, 5737 (2010).
[2] V. Jacques, P. Neumann, J. Beck, M. Markham, D. Twitchen, J. Meijer, F. Kaiser, G. Balasubramanian, F. Jelezko, and J. Wrachtrup, Phys. Rev. Lett. **102**, 057403 (2009).
[3] R. Fischer, C. O. Bretschneider, P. London, D. Budker, D. Gershoni, and L. Frydman, Phys. Rev. Lett. **111**, 057601 (2013).
[4] H.-J. Wang, C. S. Shin, C. E. Avalos, S. J. Seltzer, D. Budker, A. Pines, and V. S. Bajaj, Nat. Commun. **4**, 1940 (2013).
[5] A. L. Falk, P. V. Klimov, V. Ivády, K. Szász, D. J. Christle, W. F. Koehl, Á. Gali, and D. D. Awschalom, Phys. Rev. Lett. **114**, 247603 (2015).
[6] D. Lee, E. Bouleau, P. Saint-Bonnet, S. Hediger, and G. De Paëpe, J. Magn. Res. **264**, 116 (2016).
[7] M. Kaplan, A. Cukkemane, G. C. P. van Zundert, S. Narasimhan, M. Daniëls, D. Mance, G. Waksman, A. M. J. J. Bonvin, R. Fronzes, G. E. Folkers, and M. Baldus, Nat. Methods **12**, 649 (2015).
[8] K. Tateishi, M. Negoro, S. Nishida, A. Kagawa, Y. Morita, and M. Kitagawa, Proc. Natl. Acad. Sci. USA **111**, 7527 (2014).
[9] J. P. King, K. Jeong, C. C. Vassiliou, C. S. Shin, R. H. Page, C. E. Avalos, H.-J. Wang, and A. Pines, Nat. Commun. **6**, 8965 (2015).
[10] A. B. Siemer, K. Y. Huang, and A. E. McDermott, PLoS One **7**, e47242 (2012).
[11] E. Scott, M. Drake, and J. A. Reimer, J. Magn. Res. **264**, 154 (2016).
[12] B. L. Green, B. G. Breeze, and M. E. Newton, J. Phys.: Condens. Matter **29**, 225701 (2017).
[13] A. Cox, M. E. Newton, and J. M. Baker, J. Phys.: Condens. Matter **6**, 551 (1994).
[14] R. G. Farrer, Solid State Commun. **7**, 685 (1969).
[15] F. J. Heremans, G. D. Fuchs, C. F. Wang, R. Hanson, and D. D. Awschalom, Appl. Phys. Lett. **94**, 152102 (2009).
[16] J. Isberg, A. Tajani, and D. J. Twitchen, Phys. Rev. B **73**, 245207 (2006).

[17] R. Jones, J. Goss, and P. Briddon, Phys. Rev. B **80**, 033205 (2009).
[18] M. K. Atumi, Ph.D. thesis, Newcastle University, 2014.
[19] W. A. Runciman, Proc. Phys. Soc. **86**, 629 (1965).
[20] P. Crowther and P. Dean, J. Phys. Chem. Solids **28**, 1115 (1967).
[21] G. Davies, C. Welbourn, and J. H. N. Loubser, Diam. Res. 23 (1978).
[22] J. A. van Wyk, J. Phys. C: Solid State Phys. **15**, L981 (1982).
[23] J. A. van Wyk and J. H. N. Loubser, J. Phys.: Condens. Matter **5**, 3019 (1993).
[24] C. Coulson and M. Kearsley, Proc. R. Soc. A **241**, 433 (1957).
[25] C. Coulson and F. Larkins, J. Phys. Chem. Solids **32**, 2245 (1971).
[26] R. Jones, J. P. Goss, P. R. Briddon, and S. Öberg, Phys. Rev. B **56**, R1654 (1997).
[27] D. Fisher and A. Fitch, Diamond Conference, University of Warwick, Coventry, UK (unpublished).
[28] Y. Mita, H. Kanehara, Y. Nisida, and M. Okada, Philos. Mag. Lett. **76**, 93 (1997).
[29] B. L. Green, M. W. Dale, M. E. Newton, and D. Fisher, Phys. Rev. B **92**, 165204 (2015).
[30] J. Heyd, G. E. Scuseria, and M. Ernzerhof, J. Chem. Phys. **118**, 8207 (2003).
[31] P. Deák, B. Aradi, T. Frauenheim, E. Janzén, and A. Gali, Phys. Rev. B **81**, 153203 (2010).
[32] A. Gali, E. Janzén, P. Deák, G. Kresse, and E. Kaxiras, Phys. Rev. Lett. **103**, 186404 (2009).
[33] M. Gajdoš, K. Hummer, G. Kresse, J. Furthmüller, and F. Bechstedt, Phys. Rev. B **73**, 045112 (2006).
[34] S. B. Zhang and J. E. Northrup, Phys. Rev. Lett. **67**, 2339 (1991).
[35] C. Freysoldt, J. Neugebauer, and C. G. Van de Walle, Phys. Rev. Lett. **102**, 016402 (2009).
[36] C. Freysoldt, J. Neugebauer, and C. G. Van de Walle, Phys. Status Solidi B **248**, 1067 (2011).
[37] Z. Bodrog and A. Gali, J. Phys.: Condens. Matter **26**, 015305 (2014).
[38] V. Ivády, T. Simon, J. R. Maze, I. A. Abrikosov, and A. Gali, Phys. Rev. B **90**, 235205 (2014).
[39] O. V. Yazyev, I. Tavernelli, L. Helm, and U. Röthlisberger, Phys. Rev. B **71**, 115110 (2005).
[40] K. Szász, T. Hornos, M. Marsman, and A. Gali, Phys. Rev. B **88**, 075202 (2013).
[41] K. Saeedi, S. Simmons, J. Z. Salvail, P. Dluhy, H. Riemann, N. V. Abrosimov, P. Becker, H.-J. Pohl, J. J. L. Morton, and M. L. W. Thewalt, Science **342**, 830 (2013).
[42] M. Pfender, N. Aslam, P. Simon, D. Antonov, G. Thiering, S. Burk, F. F. de Oliveira, A. Denisenko, H. Fedder, J. Meijer, J. A. Garrido, A. Gali, T. Teraji, J. Isoya, M. W. Doherty, A. Alkauskas, A. Gallo, A. Grüneis, P. Neumann, and J. Wrachtrup, arXiv:1702.01590.
[43] See Supplemental Material at http://link.aps.org/supplemental/10.1103/PhysRevB.96.054101 for model details, sensitivities, and correction for population loss due to charge transfer.
[44] K.-N. Hu, G. T. Debelouchina, A. A. Smith, and R. G. Griffin, J. Chem. Phys. **134**, 125105 (2011).
[45] E. C. Reynhardt and G. L. High, J. Chem. Phys. **109**, 4090 (1998).
[46] H. S. Knowles, D. M. Kara, and M. Atatüre, Phys. Rev. Lett. **117**, 100802 (2016).
[47] J. P. King, P. J. Coles, and J. A. Reimer, Phys. Rev. B **81**, 073201 (2010).
[48] J. Walker, Rep. Prog. Phys. **42**, 1605 (1979).
[49] P. Delaney, J. C. Greer, and J. A. Larsson, Nano Lett. **10**, 610 (2010).
[50] V. Ivády, K. Szász, A. L. Falk, P. V. Klimov, D. J. Christle, E. Janzén, I. A. Abrikosov, D. D. Awschalom, and A. Gali, Phys. Rev. B **92**, 115206 (2015).
[51] S. Felton, A. M. Edmonds, M. E. Newton, P. M. Martineau, D. Fisher, D. J. Twitchen, and J. M. Baker, Phys. Rev. B **79**, 075203 (2009).
[52] S. Felton, A. M. Edmonds, M. E. Newton, P. M. Martineau, D. Fisher, and D. J. Twitchen, Phys. Rev. B **77**, 081201(R) (2008).
[53] C. A. Meriles and M. W. Doherty, Appl. Phys. Lett. **105**, 022403 (2014).
[54] M. W. Doherty, C. A. Meriles, A. Alkauskas, H. Fedder, M. J. Sellars, and N. B. Manson, Phys. Rev. X **6**, 041035 (2016).
[55] G. J. Hill, J. Wu, and M. J. R. Hoch, Hyperfine Interact. **120-121**, 81 (1999).
[56] J. Scheuer, I. Schwartz, Q. Chen, D. Schulze-Sünninghausen, P. Carl, P. Höfer, A. Retzker, H. Sumiya, J. Isoya, B. Luy, M. B. Plenio, B. Naydenov, and F. Jelezko, New J. Phys. **18**, 013040 (2016).
[57] A. Schweiger and G. Jeschke, *Principles of Pulse Electron Paramagnetic Resonance Spectroscopy* (Oxford University Press, Oxford, 2001).
[58] M. Batel, A. Däpp, A. Hunkeler, B. H. Meier, S. Kozerke, and M. Ernst, Phys. Chem. Chem. Phys. **16**, 21407 (2014).